Pore-Scale Mechanisms for Spectral Induced Polarization of Calcite Precipitation Inferred from Geo-Electrical Millifluidics

Satoshi Izumoto, Johan Alexander Huisman, Egon Zimmermann, Joris Heyman, Francesco Gomez, Hervé Tabuteau, Romain Laniel, Harry Vereecken, Yves Méheust, Tanguy Le Borgne

Pore-scale mechanisms for spectral induced polarization of calcite precipitation inferred from geo-electrical millifluidics

Satoshi Izumoto[1,2*], Johan Alexander Huisman[1], Egon Zimmermann[3], Joris Heyman[2], Francesco Gomez[2], Herve Tabuteau[4], Romain Laniel[4], Harry Vereecken[1] , Yves Méheust[2], and Tanguy Le Borgne[2]

[1] Agrosphere (IBG-3), Institute of Bio- and Geosciences, Forschungszentrum Jülich, Jülich, 52425, Germany

[2] Univ. Rennes, CNRS, Géosciences Rennes, UMR 6118, Rennes, 35042, France

[3] Electronic Systems (ZEA-2), Central Institute for Engineering, Electronics and Analytics, Forschungszentrum Jülich, Jülich, 52425, Germany

[4] Institute de Physique de Rennes, Université de Rennes 1, CNRS, Rennes, 35042, France

Corresponding author: Satoshi Izumoto (satoshi.izumoto@hotmail.co.jp)

[*]Address: Géosciences Rennes, UMR 6118, CNRS, Université de Rennes 1, Rennes Cedex 35042, France

Abstract

Spectral induced polarization (SIP) has potential for monitoring reactive processes in the subsurface. While strong SIP responses have been measured in response to calcite precipitation, their origin and mechanism remains debated. Here we present a novel geo-electrical millifluidic setup designed to observe microscale reactive transport processes while performing SIP measurements. We induced calcite precipitation by injecting two reactive solutions into a porous medium, which led to highly localized precipitates at the mixing interface. Strikingly, the amplitude of the SIP response increased by 340% during the last 7% increase in precipitate volume. Furthermore, while the peak frequency in SIP response varied spatially over one order of magnitude, the crystal size range was similar along the front, contradicting assumptions in the classical grain polarization model. We argue that the SIP response of calcite precipitation in such mixing fronts is governed by Maxwell-Wagner polarization due to the establishment of a precipitate wall. Numerical simulations of the electric field suggested that spatial variation in peak frequency was related to the macroscopic shape of the front. These findings provide new insights into the SIP response of calcite precipitation and highlight the potential of geoelectrical millifluidics for understanding and modelling electrical signatures of reactive transport processes.

Keywords : Complex conductivity, Calcium carbonate, Mixing, Reactive transport, Porous media, Chargeability, Maxwell-Wagner polarization, Heterogeneity

Synopsis : Using a new technology called geo-electrical millifluidics, we uncovered the microscale reactive transport mechanisms driving SIP, a promising geophysical technique for monitoring soil biogeochemical processes.

Graphical abstract

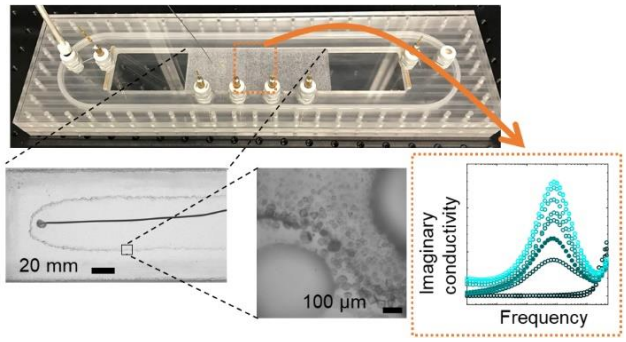

1 Introduction

Calcite ($CaCO_3$) is one of the most common minerals in the subsurface[1]. It can be formed from the calcium ion and dissolved carbon dioxide, which are major components in groundwater[1]. Calcite precipitation can cause undesirable effects, such as well clogging due to the reduction of hydraulic conductivity[2,3]. It has also been successfully used in geotechnical applications of microbially-induced calcite precipitation (MICP) such as bioremediation[4,5], stabilization of soil[6,7] and the reduction of fracture permeability[8,9]. The dynamics of calcite precipitation are usually assessed by measuring hydraulic pressure, analysing sampled pore water, or performing cone penetration tests[2–9]. However, such methods only provide information on selected points in space and time. Geophysical methods allow for non-invasive imaging of the subsurface with higher spatial and temporal resolution. Spectral induced polarization (SIP) has shown potential to detect biogeochemical processes[10–14], including calcite precipitation, in laboratory[15–18] and field measurements[19,20]. SIP measures the voltage between selected positions in the geological material while injecting a sinusoidal current in the mHz to kHz frequency range[21,22]. Due to an external electric field, the charges in the material accumulate under geometric constraints (induced polarization) [21,22]. The main purpose of an SIP measurement is to detect this process. For this, the measured voltage is processed to obtain the phase shift between the applied current and the measured voltage φ, the magnitude of the electrical conductivity $|\sigma|$, and finally the complex conductivity σ^*:

$$\sigma^* = |\sigma| e^{-i\varphi} = \sigma' + i\sigma'' \,. \tag{1}$$

In the absence of a conductive solid phase, the real part of the conductivity (σ') results from the electrolytic conduction in the water-filled pore space and along solid surfaces whereas the imaginary part of the conductivity (σ'') corresponds to the induced polarization.

A range of studies have used SIP measurements to detect precipitation of a conductive mineral phase[23–26], but relatively few studies have investigated the SIP response of calcite precipitation[15–17,27,28]. These previous studies share the common limitation that the temporal development and spatial distribution of calcite precipitation was inaccessible due to the opaque nature of the porous media used in the column experiments. However, precipitation is a dynamic process which only occurs when the pore solution is oversaturated. Thus, it is important to investigate what characteristics of the calcite precipitation process control the SIP response in the presence of spatially heterogeneous calcite precipitation.

Here we present a geo-electrical millifluidic experiment coupling SIP monitoring with pore scale imaging to investigate how spatially-variable and temporally-dynamic calcite precipitation processes affect the SIP response. To this aim, we have combined a millimetre scale 2D porous medium[29–31] and electrodes for SIP measurements to visually observe calcite precipitation at the pore scale while monitoring SIP (i.e. a millifluidic setup). Based on the experimental results, we simulated the electric field distribution in the 2D millifluidic setup to support the interpretation of the measured SIP response. Finally, we present a simple electric circuit model to provide a qualitative mechanistic explanation for the observed SIP response of calcite precipitation.

2 Materials and methods

The experimental setup consists of (1) a millifluidic setup consisting of a sample holder, 2D porous medium and electrodes connected to the SIP measurement system and (2) equipment for visualization of pore-scale processes (Figure 1a), as described in the following.

2.1 Sample holder

The sample holder was made of transparent poly(methyl methacrylate) (PMMA) with a large rectangular cavity (length: 300 mm, width: 50 mm, height 11 mm) (Figure 1b,c. See technical drawings in Supplementary Figure S1). It has two fluid injection ports on one side and in the middle of the cavity, and a fluid outlet port on the other side. Two current electrodes made of porous brass (length: 49.1 mm, width: 6.3 mm, depth: 3.7 mm) (Figure 1b) were positioned on both sides of the large rectangular cavity and completely retracted in the top plate to avoid disturbance of the water flow. Four potential electrodes made of brass (diameter of 6.5 mm) were held by water-tight cable glands in the top plate (Figure 1b). They were positioned on one side of the porous medium with equal spacing (33 mm). The measurement system of Zimmermann et al.[32] was used for SIP measurements. The measurement frequency range was from 1 Hz to 45 kHz, and the injected voltage was 5V. We do not expect nonlinear effect by this voltage (see Supplementary section 1.1). In the frequency range above 100 Hz, the parasitic capacitance of the measurement system can have significant impact on the measurement[33]. To evaluate this effect, we considered the parasitic capacitance of our measurement system during data processing[32,34]. The SIP response can be measured in different zones by choosing different pairs of potential electrodes. Further information on the sample holder is provided in Supplementary section 1.1.

2.2 2D porous medium

A fabrication method akin to soft lithography, a method commonly used to make microfluidic flow cells[35], was used to produce a 2D porous medium whose solid grains are cylindrical pillars made of Polydimethylsiloxane (PDMS) (Figure 1d, length: 12.5 mm, width: 50 mm, height: 11.6 mm, pillar height: 1 mm). The resulting porosity was 0.59. The grain size ranged between 0.34 and 0.82 mm, with a median grain size of 0.53 mm (see further details in Supplementary section 1.2 and Figure S2).

2.3 Visualization of pore-scale processes

To monitor calcite precipitation at different spatial scales, two different cameras were used (Figure 1a) in combination with a homogeneous backlight (LFL-180BL2, CCS inc., Kyoto, Japan). The first camera was a mirrorless digital camera (14-bit, SONY alpha7s, SONY, Tokyo, Japan) equipped with a macro lens (MACRO GOSS F2.8/90, SONY, Tokyo, Japan), which resulted in a field of view of 16.6×11.0 cm^2 and an image resolution of 0.03×0.03 mm^2. This "overview" camera was connected to a PC through a voltage output module (National Instruments, Austin, TX) to enable automatic image acquisition. The second camera (denoted "close-view" camera) was a high-sensitivity scientific CMOS camera (16-bit, Hamamatsu ORCA flash 4.0, Hamamatsu Photonics K.K., Shizuoka, Japan) equipped with a set of lenses (6.5X zoom lens with 2X extension tube and 1.5X lens attachment, Thorlab, Inc., Newton, MA, USA) to obtain close-up images. The field of view was 750×750 μm and the image resolution was 0.37×0.37 μm^2. This camera was fixed on a 3-axis table (Edmund Optics Ltd., Barrington, USA), which was mounted on a 2-axis motorized table constructed from two 1-axis motorized tables (Edmund Optics Ltd., Barrington, USA and Thorlab, Inc., Newton, MA, USA) controlled by a custom-made Matlab program (Mathworks, Natick, MA, USA). This allowed automatic positioning of the close-view camera to monitor selected positions with regular space intervals. Composite images were created using the open-source image processing program ImageJ with the plugin TrackEM2 (https://imagej.net/TrackEM2).

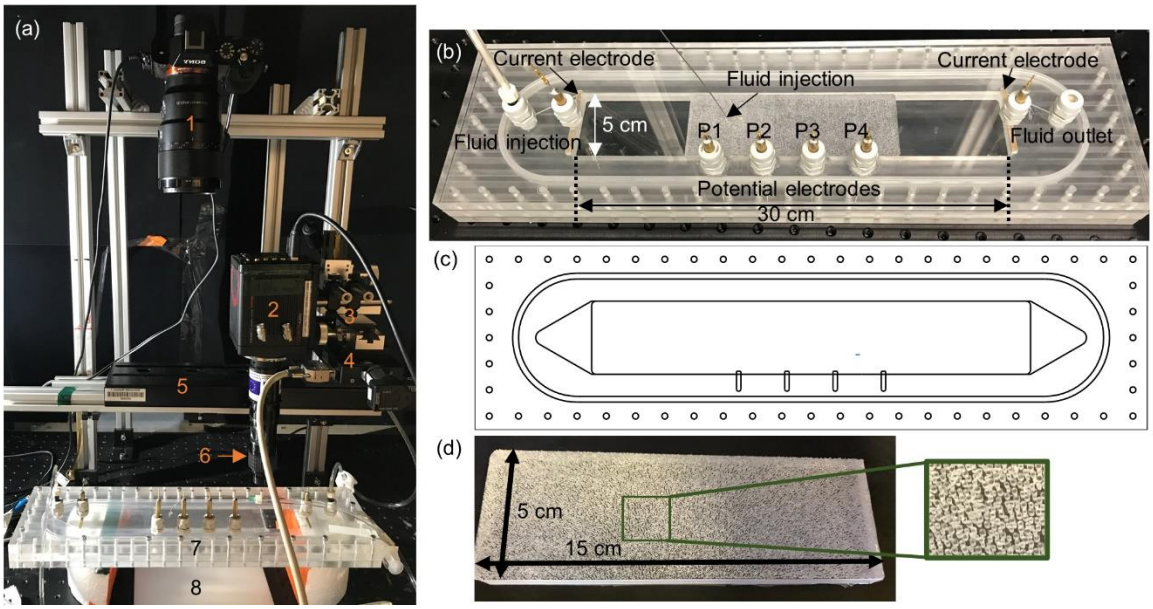

Figure 1. Overview of the experimental setup: (a) Entire setup including 1) overview camera, 2) close-view camera, 3,4) 3-axis stage, 5) 2-axis moving table, 6) lenses, 7) millifluidic setup, 8) backlight, (b) sample holder with porous medium and electrodes (see Supplementary Figure S1 for actual position of porous medium in the experiment), (c) plan view of the middle plate of the sample holder, and (d) 2D porous medium made of PDMS.

2.4 Experimental procedure

A first millifluidic calcite precipitation experiment was performed with a total duration of 80 hours using the same solute concentrations as in previous column studies[15,28]. The sample holder was first filled with a 26.2 mM $CaCl_2$ solution. Next, the same solution was injected through the injection port at the side of the 2D porous medium, and a 29 mM Na_2CO_3 solution was injected through the injection port in the middle of the porous medium (Fig. 1b). Both solutions were injected with the same flow rate (4 mL h^{-1}) using a syringe pump (model 22, Harvard Apparatus, Inc., Holliston, MA, USA). The Péclet number, which characterizes the ratio of the characteristic diffusion and advection times, is defined as $Pe = vL/D$, where v is the average velocity downstream of the injection ports, L is the average pore throat size of the porous medium and D is the molecular diffusion coefficient. The selected experimental parameters ($v = 3.86 \times 10^{-5}$ m s^{-1}, $L = 3.63 \times 10^{-4}$ m, $D = 10^{-9}$ m^2 s^{-1}) yield $Pe = 14$. This corresponds well with the order of magnitude of many applications[36,37].

Mixing between the Na_2CO_3 and $CaCl_2$ solutions induced calcite precipitation according to:

$$Ca^{2+} + CO_3^{2-} \rightarrow CaCO_3(s) \quad (2)$$

This is the approximated equation of the two-step reaction in our highly oversaturated system: formation of amorphous calcium carbonate (ACC) and subsequent crystallization[38]. When the two solutions mix, ACC quickly forms (within seconds[38]), sinks because of its high density (2.18 g cm^{-3})[39] and crystalizes to calcite (timescale ~10^4 s[40]). The Damköhler number, which characterizes the relative strength of reaction and advection, is defined as $Da = \tau_a/\tau_r$, where τ_a and τ_r are the characteristic advection and reaction times, respectively. The advection time is $\tau_a = L/v = 9.4$ s, with $L = 3.63 \times 10^{-4}$ m the average pore throat size and $v = 3.86 \times 10^{-5}$ m s^{-1} the mean velocity downstream of the injection point. We approximated the characteristic time for ACC formation as 5 s based on visual observations when mixing the solutions. By taking this ACC formation time as a characteristic reaction rate, the Damköhler number is about $Da \approx 2$, which indicates that reactions are fast compared to the advective transport.

SIP measurements were made in three measurement zones, which will be referred to as the upstream, middle, and downstream measurement zone, using the electrode pairs P1 and P2, P2 and P3, and P3 and P4, respectively (Figure 1b). To capture the early formation of the precipitation front, we measured more frequently in the upstream zone (every 18 minutes) than in other zones (every 8 hours). Images were taken every 8 minutes with the overview camera and with the close-view camera for four selected horizontal positions. Two of these positions were located in the upstream zone and the two other positions were located in the middle and downstream zones. At each position, the close-view camera took 10×10 images with a regular space interval using the motorized stage, which resulted in a composite image size of 7.5 mm × 7.5 mm. At the end of the experiment, the close-view camera took images of the entire zone with calcite precipitates.

After the flow experiment, the 2D porous medium was removed from the sample holder to measure the height of the precipitate using a profilometer (Altisurf 500, Altimet, France) with a vertical resolution of 5 μm and a horizontal resolution of 50 μm. A calibration function was established to relate the image grey levels and the height of the precipitate (further details are given in section 1.3 of the Supplementary Information and Figure S3). After the calibration, the calcite precipitates were observed using a microscope with 10X and 40X lenses (Inverted Laboratory Microscope, Leica microsystems, Cambridge, United Kingdom).

The SIP response obtained during injection of $CaCl_2$ and Na_2CO_3 solutions is potentially affected by spatial and temporal variations in solute concentration[28] because of the ongoing

precipitation reactions. To investigate the effect of such variations, we performed a second experiment in which the injected reactive solutions were replaced by a single, non-reactive solution during two time periods. By this replacement, the solute concentration becomes spatially homogeneous. To prepare the replacement solution, a 26.2 mM $MgCl_2$ solution and a 29.0 mM Na_2CO_3 solution were mixed and centrifuged to remove any $MgCO_3$ precipitates. This mixed solution was expected to be non-reactive with calcite precipitates and to induce a relatively large SIP response due to the presence of Mg^{2+} and CO_3^{2-} ions[41] (see section 1.4 of the Supplementary Information for more details). We call this mixed solution the $MgCO_3$ solution. The experimental approach was the same as in the first experiment up to 47 h: calcite precipitation was first induced by injecting $CaCl_2$ solution and Na_2CO_3 solutions, and the precipitation was visually monitored while making SIP measurements. After 47 h, the two injected solutions were changed to the $MgCO_3$ solution. After the SIP response stabilized in response to the injection of $MgCO_3$ solution (after ~16 pore volumes), the original Na_2CO_3 and $CaCl_2$ solutions were injected again. About 27 pore volumes of Na_2CO_3 and $CaCl_2$ solution were sufficient to obtain a SIP response similar to the response before the injection of $MgCO_3$ solution. The same procedure was repeated after 87.5 h. This procedure provided the SIP response of calcite with a spatially homogeneous solute concentration at two different times (47 h and 87.5 h).

2.5 Simulation

To investigate how the spatial distribution of the calcite precipitates affects the SIP measurements, electrical field simulations were performed with a custom-made finite-element modelling approach implemented in Matlab (Mathworks, Natick, MA, USA). The governing equation is:

$$\boldsymbol{\nabla} \cdot \boldsymbol{J} = \boldsymbol{\nabla} \cdot (\sigma^* \boldsymbol{\nabla} \Phi^*) \,, \tag{3}$$

where J is current density (A m^{-2}), Φ^* is the complex potential (V) and σ^* is the complex conductivity (S m^{-1}). The modelling domain was the rectangular area between the current electrodes (30 cm × 5 cm), which was discretised in right-angled triangles with a base and side length of 2 mm. Because it was not computationally feasible to use a mesh sufficiently fine to resolve the pore scale, a Darcy-scale approach had to be used with effective properties assigned to different areas[42]. Thus, the simulations were only used to analyse qualitative trends. The effective electrical conductivity of the background was determined from the solute concentration and the formation factor. The shape of the area with calcite precipitates was

obtained from images of the overview camera. A modified Cole-Cole model[42] describes the effective complex conductivity of this area :

$$\sigma^* = (1-m)R_\sigma\sigma_{\text{bulk}}\frac{1}{1-m\left(1-\frac{1}{1+(2\pi fTi)^c}\right)} \quad (4)$$

where m is the chargeability, f is the frequency (Hz), T is the characteristic time (s), c is a shape exponent and R_σ defines the ratio between the high-frequency limit of the conductivity, σ_∞, and the bulk conductivity σ_{bulk}:

$$R_\sigma = \frac{\sigma_\infty}{\sigma_{\text{bulk}}} < 1 \quad (5)$$

Electric current without imaginary part was applied at the right boundary (see Eq.3) and the current ejected from the left boundary. The potentials were determined at the positions identical to those of the voltage measurements in the experiments. The parameters and simulation domains were based on the experimental results (section 3.3.1).

3 Results and discussion

3.1 Precipitation process

The large-scale images show that the front develops as a continuous region, which becomes darker over time at the boundary between the two injected solutions (Figure 2a). The shape of this boundary corresponds with the streamlines of the Rankine half-body potential flow[43]. The composite images obtained from the close-view camera (Figure 2a, middle and right column) successfully captured the development of individual crystals (also see section 2.1 of the Supplementary Information, Figure S4, S5 and Movie S1). Calcite precipitation created a solid wall along the mixing interface without visible pores at 0.16×0.16 μm^2 resolution (Figure 2b). This likely occurred because the amorphous calcium carbonate settled on the bottom plate due to its higher density and could attach on calcite surfaces that were already present. Further details are provided in section 2.2 of the Supplementary Information and Figure S6 therein.

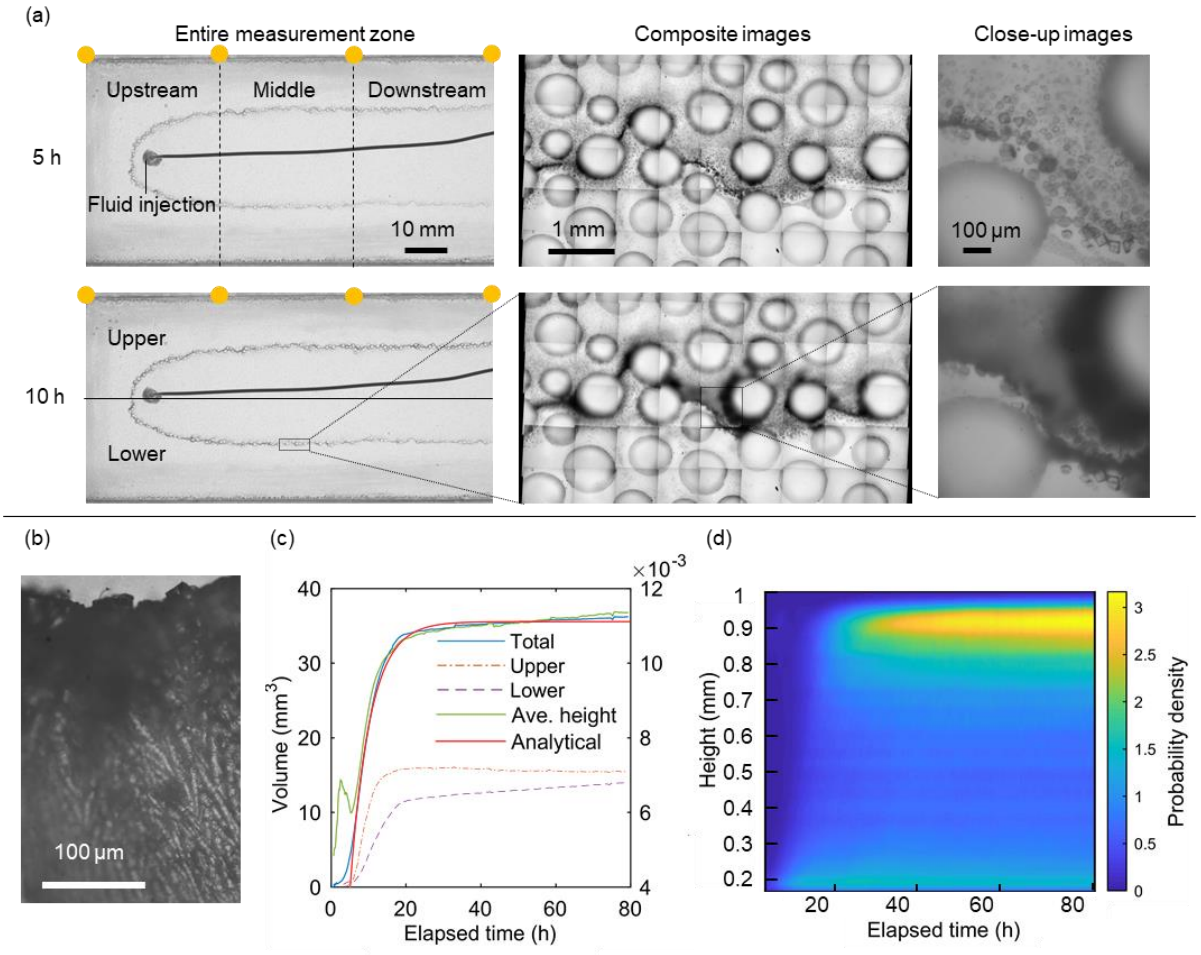

Figure 2. (a) Digital images of the entire measurement area taken at different times (left column), composite images of a selected area along the calcite precipitation front (center column), and calcite crystals in close-up images (right column). The yellow dots indicate the position of the electrodes. The black line connected to the fluid injection port is the tubing. (b) Side view of the calcite wall. (c) Change in volume of precipitate over time in the entire measurement zone as well as in the upper (near the potential electrodes) and lower half of the sample holder in Figure 2a; the change in mean precipitate height for the entire domain is superimposed on that of the volume. (d) Spatio-temporal diagram showing the time evolution of the V_f-normalized PDF of the precipitate heights (V_f being the final volume of precipitate).

In a next step, we quantified the relationship between the grey level of the image and the height of the precipitate from the profilometer. This correlation was found to be relatively good with a small spread of data. The tendency was well fitted by an arctangent function, which captured most data points within ±0.1 mm (section 1.3 of the Supplementary Information and Figure

S3). Because calcite did not have pores (Figure 2b), this calibration curve can be used to obtain the spatial distribution of the total volume of precipitate from the grey level in the overview images. It was found that both the volume and the mean height increased up to 20 h, followed by relatively constant value (Figure 2c). This suggests that the surface area of the reactive zone is relatively constant and that the quick increase in volume in the first 20 hours can be attributed to the rise of the calcite wall. Note that the peak of the volume change in early time was probably because the amorphous phase started to crystalize at this time. Figure 2d shows the time evolution of the probability density function (PDF) of precipitate heights. Note that only the final PDF is normalized to 1 as a standard PDF and that the entire data set has the same normalization factor as this final PDF. Figure 2d thus shows the relative evolution of the height histogram with time, and we denote them "V_f-normalized PDFs". The PDF has a strong peak around 0.9 mm after 20h. This peak corresponds to the height of the solid calcite precipitate wall, whereas the lower height corresponds to the stacked calcite crystals surrounding the calcite wall (Supplementary Figure S6). This analysis also shows that the height only increased further in areas where a high wall of precipitation was already present after 20 h (i.e. a continued vertical development of the calcite wall). Because of the differences in the development of calcite precipitation before and after 20 h (Figure 2c,d), these two periods will be considered separately in the following.

The observed reduced speed of calcite precipitation with time can be understood conceptually. The calcite precipitation divided the two injected fluids and precipitation is expected to occur in the mixing zone (Supplementary Figure S7). As the height of the calcite precipitation increases, the size of this mixing zone is reduced[44]. This leads to a decrease in the reaction rate and a reduced growth of the height of the calcite precipitates. This feedback mechanism between the reaction rate and the height of the calcite precipitates thus leads to a slow but continuous growth of the volume of calcite precipitates even after 20 h. By considering the diffusive flux toward the calcite wall in combination with this feedback mechanism, we developed an analytical model that predicts the change in volume with time (section 2.3 of the Supplementary Information). This model was able to describe the observed volume (Figure 2c), which supports the notion that the described feedback mechanism controls mixing and precipitation.

3.2 SIP response

Calcite precipitation generally resulted in an increase of the imaginary part of conductivity σ'' (Figure 3a). The comparison between the σ'' with and without correction of parasitic capacitance showed that the results were not much influenced by the parasitic capacitance below 10 kHz (Supplementary section 2.4). The measurement at time 0 h without correction (Figure 3a) also showed a low σ'' for frequencies below 10 kHz with sufficient accuracy, which again indicates that the effect of parasitic capacitances was small enough in this frequency range. Hence, uncorrected data were used for further analysis. In all three measurement zones, a clear peak in σ'' appeared (Figure 3a). Also, relatively strong negative σ'' values were measured in the low frequency range in the upstream measurement zone. Such negative σ'' values are not physically possible for homogeneous samples but can occur in the case of heterogeneous samples (section 3.3). We further analyzed σ'' regarding the peak value σ_p'' (Figure 3b) and the peak frequency (Figure 3c). The increase in σ_p'' was much smaller up to 20 hours than afterwards even though the volume of precipitates increased strongly in this period (Figure 3b). The value of σ_p'' strongly increased by 340% after 24 h, while the volume of the precipitates changed only slightly by 7%. This suggests that the SIP response is not only sensitive to the amount of precipitates. The peak frequency was relatively constant in time and ranged from about 200 Hz to 2 kHz depending on the measurement zone. It was larger in the upstream zone close to the injection point than in other areas (Figure 3c). The duplicated experiment showed qualitatively similar trends for all key features of the SIP response. In this duplicate experiment, it was also verified that streaming potential did not have much influence by comparing the SIP response with and without flow (Supplementary Figure S12).

According to the grain polarization model[45,46], the radius of the crystal, *r*, can be predicted from the peak frequency as:

$$r = \sqrt{2D_s M/f}\,, \tag{6}$$

where *f* is the peak frequency, D_s is the surface diffusion coefficient, which was assumed to be roughly 10 times smaller than the bulk diffusion coefficient in previous studies (10^{-10} m^2 s^{-1})[41], and *M* is a parameter accounting for the effect of the diffuse double layer, which was assumed to be 31 based on a previous study[41]. This model suggests that the mean crystal size in the downstream region (*f* = 200 Hz) should be twice as large as in the middle region (*f* = 900 Hz). However, our pore scale imaging results showed that the range of the crystal sizes was similar in all measurement zones on the same side of the Rankine half-body flow, except at the

stagnation point (Supplementary Figure S5). In addition, the largest predicted crystal radius is 5.6 µm for f = 200 Hz. We observed that most of such small crystals disappeared after 10 hours (Supplementary Movie S1) because smaller crystals are thermodynamically less stable and experience Ostwald ripening[48,49]. If such small crystals were responsible for the SIP response, σ'' should have been larger early in the experiment, which was not the case. Hence, we conclude that the grain polarization model is not able to describe this feature in our experiments.

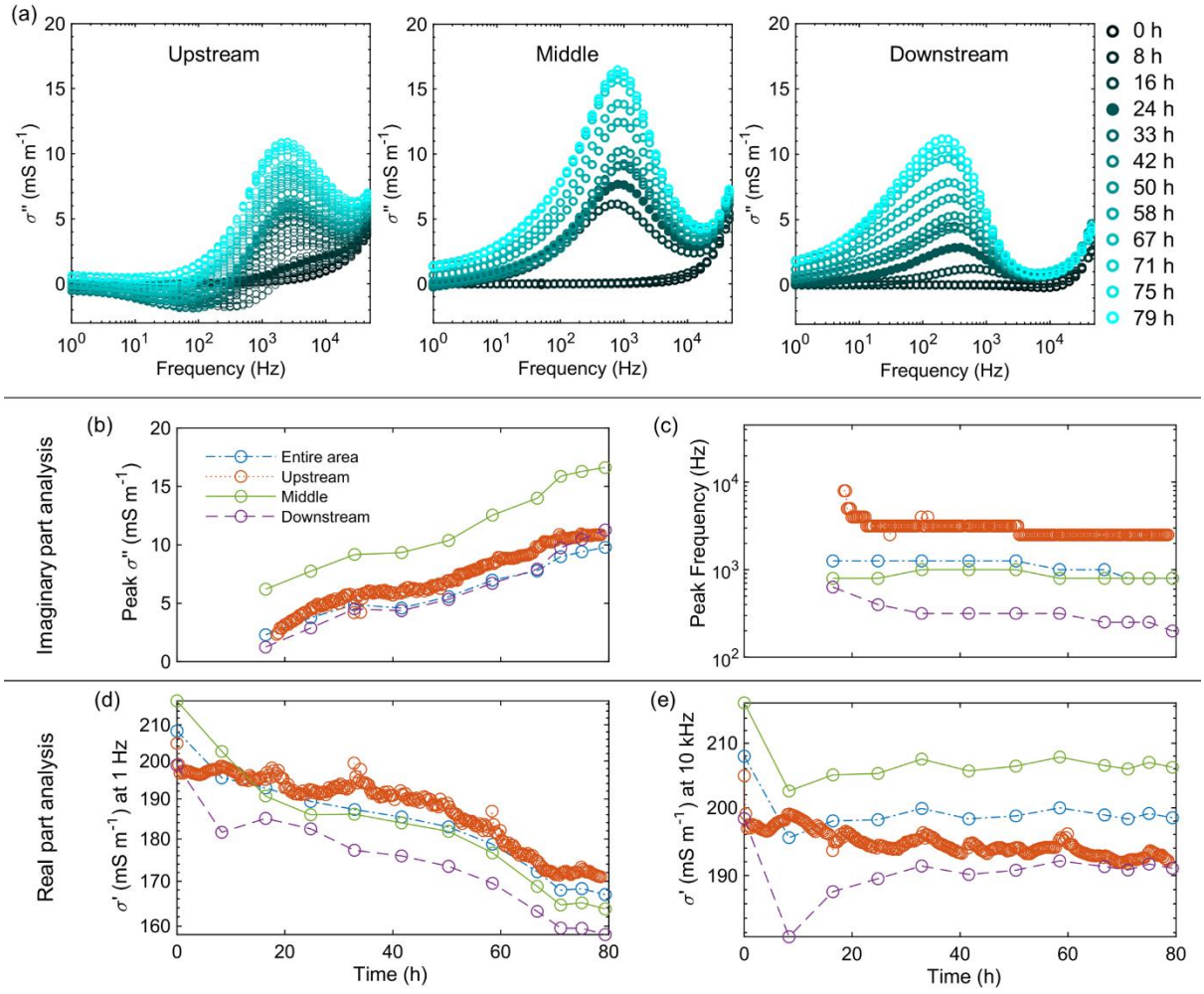

Figure 3. (a) SIP response as a function of time for the three different measurement zones and key characteristics of the SIP response as a function of time for the three measurement zones: (b) peak frequency, (e) σ'' at peak frequency, (d) σ' at 1 Hz and (e) σ' at 10 kHz. The absence of early time results in (b) and (e) is due to the absence of a peak in σ''.

The interpretation of the real part of conductivity σ' is challenging for the period before 20 h (Figure 3d,e) because the reactions strongly affect solute concentration as well as the fraction of precipitates in the solution, and therefore the conductivity (see further details in section 2.5

of the Supplementary Information and Figure S10). After 20 h, σ' at 10 kHz was almost constant and σ' at 1 Hz decreased over time. These different trends of σ' between 1 Hz and 10 kHz after 20 h are the key to understanding how the SIP response increased (more detail in section 3.3).

In the additional experiment where the sample holder was flushed twice with the $MgCO_3$ solution, the injection of $MgCO_3$ solution decreased the imaginary part of conductivity as expected from previous studies[28] and increased the peak frequencies (Figure S13 and S14). However, the SIP response after injection of $MgCO_3$ solution still showed a higher peak frequency in the upstream region, similar peak frequencies in both injection periods for each measurement zone, and a slightly larger σ'' later in the experiment. In the period between the injections of $MgCO_3$ solution, a slight increase in σ'' was observed as in the main experiment with $CaCl_2$ and Na_2CO_3 solutions only. Since the solute concentration was homogeneous due to the injection of $MgCO_3$ solution, these characteristics of the SIP response are thus not governed by a heterogeneous distribution of solute concentration.

3.3 Microscopic and macroscopic controls on SIP response

Our experiments revealed some unexpected effects of pore scale transport and reaction on the SIP response: i) a temporal lag between the peak σ'' value and the precipitation and ii) spatial variation in peak frequency. In the following, we argue that the former is related to pore scale dynamics, while the latter is governed by the macroscopic precipitate distribution.

3.3.1 Pore scale processes

The most unexpected result is that the peak σ'' value mostly increased after 20 hours (Figure 2b) while the volume of precipitates only slowly increased (Figure 3c). At the same time, σ' at 1 Hz decreased (Figure 3d) while σ' at 10 kHz was almost constant (Figure 3e). This indicates an increase in chargeability with time[42,50]. It is again difficult to explain these results with the grain polarization model for two reasons. First, the calcite wall cannot adequately be modelled by the grain polarization model because it is not a porous medium with identifiable grains but a solid precipitate (Figure 2b). Second, the grain polarization model suggests that the chargeability may increase due to an increase in surface area, changes in crystal size or an increase in the solute concentration[41]. It seems unlikely that the observed increase in chargeability can be explained by an increase in surface area or crystal size because changes in the volume of calcite precipitation were quite small after 20 h (Figure 2c) and the crystal size

did not change after 20 h (section 2.1 of the Supplementary Information). It is also unlikely that variations in solute concentration over space are responsible for the characteristics of the SIP response because the experimental results obtained with homogeneous concentration fields (section 2.7 of the Supplementary Information) showed the same key characteristics of the SIP response as those obtained with heterogeneous concentration fields, such as different peak frequencies depending on the measurement zone.

An alternative explanation for the strong increase in SIP response is that it may be associated with Maxwell-Wagner polarization associated with the thin calcite precipitation wall. Maxwell-Wagner polarization considers the entire material body as a dielectric material with a certain capacitance[22]. To test the potential importance of this source of polarization, we considered a simple conceptual model (Figure 4a) consisting of a calcite wall (length 10^{-3} mm, width 1 mm), a mixing zone above the calcite wall (length 10^{-3} mm, width 1 mm), and the surrounding water (length 5 mm, width 1 mm, height 1 mm). In the experiments, we observed a slow but continuous growth of the calcite precipitation after 20 hours and a calcite wall that almost filled the pore space in vertical direction. Thus, we specified a thin mixing zone above the calcite wall (0.01-0.0001 mm) and a high calcite wall (0.99 – 0.9999 mm). The width of the calcite wall is based on the actual dimensions of the calcite precipitation front obtained from images acquired after the experiment. The water in the mixing zone is assumed to be in equilibrium with the calcite (0.375 S m^{-1}), whereas the pore water conductivity was taken as the average of the injected solutions (0.50 S m^{-1}). The relative permittivity of calcite was assumed to be 12[51]. For simplicity, pure calcite without an electric double layer is considered here (i.e. only Maxwell-Wagner polarization).

This conceptual model can be simplified to an electric circuit model as shown in Figure 4a, in which the electrical properties (R_1, R_2, C) can be calculated based on the dimensions and parameters provided above (see section 3.1 of Supplementary Information for more details). The model suggests that an increase in calcite wall height will lead to a lower peak frequency, an increase in the peak σ'', a plateau at constant σ' at high frequencies, and a decrease in σ' at low frequencies (Figure 4b). Thus, this conceptual model is highly sensitive to the size of the gap between the top of the calcite wall and the top plate, especially when the gap is nearly closed (high R_2). This may explain why small increases in the height of the calcite precipitation resulted in large increases in chargeability after 20 h in the experiment. Also, the small σ'' before 20 h can be partly attributed to the large gap between the top plate and the calcite wall.

This simple model thus qualitatively captures some of the key characteristics of the experimental results.

The reason why the Maxwell-Wagner polarization model can describe our experiments can be further elucidated by contrasting it with the grain polarization model. If the calcite wall is modelled by the grain polarization model, the surface of the calcite (electrical double layer) is associated with a complex conductivity, but the body of the calcite crystal is purely resistive because no pores were observed. Thus, an increase in height of the calcite precipitation (increase in the volume of calcite) would decrease σ' in the entire frequency range because the non-conductive calcite crystal replaces conductive water. It is unlikely that this decrease is fully compensated by an increase in the volume of the electrical double layer because the size of the electrical double layer (a few Angström[41]) would be much smaller than that of calcite crystals if the grain polarization model is applied (µm scale, see section 3.2). In contrast, Maxwell-Wagner polarization simply considers the entire calcite crystal as a capacitance, which has zero resistance in the high frequency limit. This thus provides a straightforward explanation of why σ' decreases at low frequencies and remains constant σ' for high frequencies (Figure 3e, Figure S10).

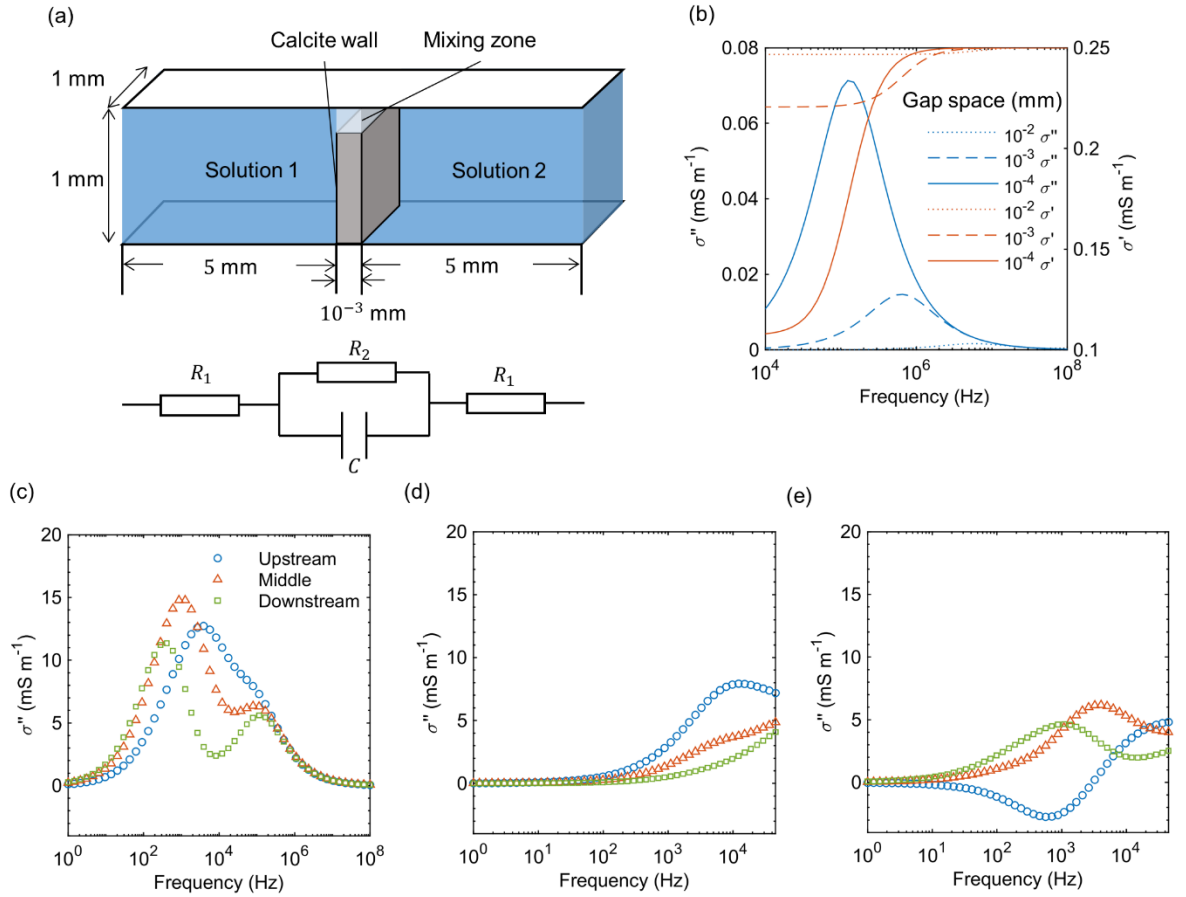

Figure 4. (a) Conceptual model to explain the Maxwell-Wagner polarization associated with the calcite precipitation front and equivalent electrical circuit of the conceptual model, (b) simulated σ'' as a function of the height of the calcite precipitation front. (c) SIP response simulated for the different measurement zones under continuous calcite precipitation front, (d) discontinuous calcite precipitation front, and (e) spatially variable complex electrical conductivity of calcite.

3.3.2 Effect of macroscopic precipitate distribution on peak frequency

A second striking result is that the peak frequency varied significantly in space while the range of crystal size did not change substantially along the mixing front except at the stagnation point (Figure S5). We hypothesized that this was due to the macroscopic spatial arrangement of the calcite precipitation. To test this, we performed electrical field simulations in three scenarios.

The first scenario corresponds to t = 20 h, where a clear and continuous precipitate wall was observed (Supplementary Figure S16a). The background electrical conductivity was 0.162 S m^{-1} based on the measured formation factor and the solute conductivity. The complex electrical conductivity of the area with calcite was defined using the modified Cole-Cole model (eq. 4).

To determine suitable parameters to reproduce the observed SIP response, simulations were run with a varying m (0.5 to 0.999) and R_σ (0.005 to 0.99). The relaxation time was fixed to 10^{-3} s. It was found that a m of 0.995 and an R_σ equal to 0.9 times the background conductivity provided a qualitatively similar SIP response as in the experiments (Supplementary Figure S17). These parameters resulted in a peak frequency at 100 kHz, which corresponds to the peak frequency near the calcite precipitation front modelled by Maxwell-Wagner polarization in section 3.3.1 (Figure 4b and Figure S19). The chosen m was two orders of magnitude higher than in a previous study[15]. This is because this previous study used a parameterization for an entire column occupied by glass beads and a small fraction of calcite, whereas we used a parameterization for a small domain mostly filled by calcite wall without pores, which is non-conductive at low frequencies. The high m also reflects the concept of Maxwell-Wagner polarization, which suggests that the calcite wall becomes fully conductive at high frequencies.

The simulation results showed that the peak frequency for the three measurement zones can be different even if the complex electrical conductivity of the calcite precipitates is the same everywhere (Figure 4c left). In particular, this occurred when both m and R_σ values were high. This likely explains why differences in peak frequency were observed between the three measurement zones, although the crystal size range was similar. Furthermore, multiple peaks in the dependence of σ'' on the frequency can occur in the middle and downstream zones with high m and R_σ values even though the specified frequency-dependent complex electrical conductivity for calcite only exhibited a single peak. Only the lower peak frequencies were in the frequency range in the experiments. Also, σ'' in the middle zone was larger than that of the two other zones (Figure 4c left), which is consistent with the experimental results.

A second simulation scenario represents a relatively early stage of the experiment where the calcite precipitate wall was not yet completely continuous (Supplementary Figure S16b). In this case, a fraction (33%) of the calcite precipitate was replaced by solution. With this discontinuous precipitation front, the simulated σ'' decreased substantially (Figure 4b middle), which suggests that σ'' is sensitive to the continuity of the precipitation front. The small σ'' before 20 h in the experiments can thus be partly attributed to the discontinuity of the calcite wall at these early times.

In a third simulation scenario, we explored how a heterogeneous distribution of the complex electrical conductivity of the calcite precipitate influences the SIP response (Supplementary Figure S16c). The experimental results suggested that calcite precipitation was slightly faster

and more abundant in the vicinity of the electrodes than elsewhere (Figure 2c), likely due to the local pore arrangement or a slight tilt of the injection tube with respect to the cell's longitudinal direction. To test the effect of this heterogeneous distribution, the chargeability was set higher for the half part of calcite that was closer to the electrodes (m=0.995) than for the calcite further away from the electrodes (m=0.4) corresponding to upper and lower part in Figure 2a (also Supplementary Figure S16c). This setting is based on the faster calcite precipitation in upper part (Figure 2c). Here, the experimental conditions after 20 h are considered again. In this case, the simulated σ'' partly showed negative values for the upstream measurement zone (Figure 4c right). Thus, heterogeneous calcite properties likely explain the observed negative σ'' values obtained in the upstream measurement zone. Further explanations about σ' and the origin of different peak frequencies can be found in section 3.2, 3.3, and 3.4 of the Supplementary Information and Figure S19, S20 and S21.

Finally, the discussed macroscopic and microscopic mechanisms also explain the reproducibility of the experiments. It was possible to precisely reproduce the observed peak frequency because it is controlled by the macroscopic shape of the reaction front, which is strongly controlled in our experimental approach. The magnitude of σ'' was less precisely reproduced because it is controlled by pore scale processes that are sensitive to local flow conditions (see section 3.5 of the Supplementary Information for more details).

4. Implications

We have developed a novel geoelectrical millifluidic system to understand the role of pore scale reactive mixing processes in the SIP response to calcite precipitation. We observed the development of a calcite precipitation front at the interface between two reactive solutions, both micro- and macroscopically, while measuring the SIP response. The calcite precipitation was highly localized at the mixing interface, which resulted in wall like calcite precipitates. The SIP response was relatively low during the early stage of the experiments, even though most of the precipitation occurred in this stage. Surprisingly, the amplitude of the SIP response increased strongly in the later stage when the calcite front was evolving much slower. Furthermore, the peak frequency of SIP response varied over one order of magnitude depending on the measurement zones without significant difference in the range of crystal size.

We proposed a pore scale electric circuit model to explain the apparent contradiction between the volume of precipitates and SIP response. By including Maxwell-Wagner polarization, the model reproduced the experimental results: the continuous filling of the gap between the top

plate of the millifluidic cell and the top of the calcite wall can increase the SIP response with only small increase in the volume of precipitates. We further simulated the electrical field in the entire measurement zone to explain the spatial variation of the peak frequencies. The simulation results showed that this variation in peak frequency is likely due to the macroscopic shape of the highly localized calcite precipitation front. In addition, these simulations showed that negative σ" values observed in the experiments may be explained by the heterogeneous development of the electrical properties of the calcite precipitates and the macroscopic discontinuity of the calcite wall largely decreases SIP response.

These findings will be useful to interpret SIP measurements in field conditions. Although our flow field (Rankine half-body) was 2D, similar 3D shapes of the reaction front are common in field conditions where a point solute source exists in a uniform groundwater flow field[52]. Even though calcite precipitation is typically induced biochemically in geotechnical applications[4,5] instead of chemically as in our experiments, the process of closing pore space also happens in such systems[20]. Therefore, our findings open new insights into the mechanisms driving the SIP response of calcite precipitation. Coupling SIP monitoring with pore scale imaging allows unravelling the contribution of different microscale processes driving the SIP response. Results highlight the importance of key pore scale and Darcy scale processes that need to be integrated in models for relating quantitatively the SIP response to reactive transport dynamics. The developed geoelectrical millifluidic system may be used in the future to investigate the role of micro-scale processes in the geoelectrical signature of a range of reactive transport dynamics.

Acknowledgements

Funding for this study was provided by European Union's Horizon 2020 research and innovation programme under the Marie Sklodowska-Curie Grant Agreement N°722028 to the project entitled "ENIGMA (European training Network for In situ imaGing of dynaMic processes in heterogeneous subsurfAce environments)".

References

(1) Drever, J. I. *The Geochemistry of Natural Waters, 3rd Ed.*; Drever, J. I., Ed.; Prentice-Hall: Englewook Cliffs, 1997.

(2) Pavelic, P.; Dillon, P. J.; Barry, K. E.; Vanderzalm, J. L.; Correll, R. L.; Rinck-Pfeiffer, S. M. Water Quality Effects on Clogging Rates during Reclaimed Water ASR in a Carbonate Aquifer. *J. Hydrol.* **2007**, *334* (1–2), 1–16. https://doi.org/10.1016/j.jhydrol.2006.08.009.

(3) Regenspurg, S.; Feldbusch, E.; Byrne, J.; Deon, F.; Driba, D. L.; Henninges, J.; Kappler, A.; Naumann, R.; Reinsch, T.; Schubert, C. Mineral Precipitation during Production of Geothermal Fluid from a Permian Rotliegend Reservoir. *Geothermics* **2015**, *54*, 122–135. https://doi.org/10.1016/j.geothermics.2015.01.003.

(4) Fujita, Y.; Taylor, J. L.; Gresham, T. L. T.; Delwiche, M. E.; Colwell, F. S.; Mcling, T. L.; Petzke, L. M.; Smith, R. W. Stimulation of Microbial Urea Hydrolysis in Groundwater to Enhance Calcite Precipitation. *Environ. Sci. Technol.* **2008**, *42* (8), 3025–3032. https://doi.org/10.1021/es702643g.

(5) Fujita, Y.; Taylor, J. L.; Wendt, L. M.; Reed, D. W.; Smith, R. W. Evaluating the Potential of Native Ureolytic Microbes to Remediate A90Sr Contaminated Environment. *Environ. Sci. Technol.* **2010**, *44* (19), 7652–7658. https://doi.org/10.1021/es101752p.

(6) Burbank, M. B.; Weaver, T. J.; Green, T. L.; Williams, B. C.; Crawford, R. L. Precipitation of Calcite by Indigenous Microorganisms to Strengthen Liquefiable Soils. *Geomicrobiol. J.* **2011**, *28* (4), 301–312. https://doi.org/10.1080/01490451.2010.499929.

(7) Gomez, M. G.; Martinez, B. C.; DeJong, J. T.; Hunt, C. E.; deVlaming, L. A.; Major, D. W.; Dworatzek, S. M. Field-Scale Bio-Cementation Tests to Improve Sands. *Proc. Inst. Civ. Eng. - Gr. Improv.* **2015**, *168* (GI3), 206–216. https://doi.org/10.1680/grim.13.00052.

(8) Cuthbert, M. O.; McMillan, L. A.; Handley-Sidhu, S.; Riley, M. S.; Tobler, D. J.; Phoenix, V. R. A Field and Modeling Study of Fractured Rock Permeability Reduction Using Microbially Induced Calcite Precipitation. *Environ. Sci. Technol.* **2013**, *47*, 13637–13643. https://doi.org/10.1021/es402601g.

(9) Phillips, A. J.; Cunningham, A. B.; Gerlach, R.; Hiebert, R.; Hwang, C.; Lomans, B. P.; Westrich, J.; Mantilla, C.; Kirksey, J.; Esposito, R.; Spangler, L. Fracture Sealing

with Microbially-Induced Calcium Carbonate Precipitation: A Field Study. *Environ. Sci. Technol.* **2016**, *50*, 4111–4117. https://doi.org/10.1021/acs.est.5b05559.

(10) Mellage, A.; Smeaton, C. M.; Furman, A.; Atekwana, E. A.; Rezanezhad, F.; Van Cappellen, P. Linking Spectral Induced Polarization (SIP) and Subsurface Microbial Processes: Results from Sand Column Incubation Experiments. *Environ. Sci. Technol.* **2018**, *52* (4), 2081–2090. https://doi.org/10.1021/acs.est.7b04420.

(11) Mellage, A.; Holmes, A. B.; Linley, S.; Vallée, L.; Rezanezhad, F.; Thomson, N.; Gu, F.; Van Cappellen, P. Sensing Coated Iron-Oxide Nanoparticles with Spectral Induced Polarization (SIP): Experiments in Natural Sand Packed Flow-Through Columns. *Environ. Sci. Technol.* **2018**, *52* (24), 14256–14265. https://doi.org/10.1021/acs.est.8b03686.

(12) Mendieta, A.; Jougnot, D.; Leroy, P.; Maineult, A. Spectral Induced Polarization Characterization of Non-Consolidated Clays for Varying Salinities—An Experimental Study. *J. Geophys. Res. Solid Earth* **2021**, *126* (4). https://doi.org/10.1029/2020JB021125.

(13) Tsukanov, K.; Schwartz, N. Modeling Plant Roots Spectral Induced Polarization Signature. *Geophys. Res. Lett.* **2021**, *48* (5), 1–8. https://doi.org/10.1029/2020GL090184.

(14) Schwartz, N.; Levy, L.; Carmeli, B.; Radian, A. Spectral Induced Polarization of Clay-Oxide Hybrid Particles. *J. Colloid Interface Sci.* **2020**, *577*, 173–180. https://doi.org/10.1016/j.jcis.2020.05.029.

(15) Wu, Y.; Hubbard, S.; Williams, K. H.; Ajo-Franklin, J. On the Complex Conductivity Signatures of Calcite Precipitation. *J. Geophys. Res. Biogeosciences* **2010**, *115* (G2), G00G04. https://doi.org/10.1029/2009JG001129.

(16) Wu, Y.; Ajo-Franklin, J. B.; Spycher, N.; Hubbard, S. S.; Zhang, G.; Williams, K. H.; Taylor, J.; Fujita, Y.; Smith, R. Geophysical Monitoring and Reactive Transport Modeling of Ureolytically-Driven Calcium Carbonate Precipitation. *Geochem. Trans.* **2011**, *12* (7). https://doi.org/10.1186/1467-4866-12-7.

(17) Saneiyan, S.; Ntarlagiannis, D.; Werkema, D. D.; Ustra, A. Geophysical Methods for Monitoring Soil Stabilization Processes. *J. Appl. Geophys.* **2018**, *148*, 234–244. https://doi.org/10.1016/j.jappgeo.2017.12.008.

(18) Redden, G.; Fox, D.; Zhang, C.; Fujita, Y.; Guo, L.; Huang, H. CaCO3 Precipitation, Transport and Sensing in Porous Media with in Situ Generation of Reactants. *Environ. Sci. Technol.* **2014**, *48* (1), 542–549. https://doi.org/10.1021/es4029777.

(19) Saneiyan, S.; Ntarlagiannis, D.; Ohan, J.; Lee, J.; Colwell, F.; Burns, S. Induced Polarization as a Monitoring Tool for In-Situ Microbial Induced Carbonate Precipitation (MICP) Processes. *Ecol. Eng.* **2019**, *127*, 36–47. https://doi.org/10.1016/j.ecoleng.2018.11.010.

(20) Saneiyan, S.; Ntarlagiannis, D.; Colwell, F. Complex Conductivity Signatures of Microbial Induced Calcite Precipitation, Field and Laboratory Scales. *Geophys. J. Int.* **2020**, 51–87. https://doi.org/10.1093/gji/ggaa510.

(21) Kessouri, P.; Furman, A.; Huisman, J. A.; Martin, T.; Mellage, A.; Ntarlagiannis, D.; Bücker, M.; Ehosioke, S.; Fernandez, P.; Flores-Orozco, A.; Kemna, A.; Nguyen, F.; Pilawski, T.; Saneiyan, S.; Schmutz, M.; Schwartz, N.; Weigand, M.; Wu, Y.; Zhang, C.; Placencia-Gomez, E. Induced Polarization Applied to Biogeophysics: Recent Advances and Future Prospects. *Near Surf. Geophys.* **2019**, *17* (6), 595–621. https://doi.org/10.1002/nsg.12072.

(22) Kemna, A.; Binley, A.; Cassiani, G.; Niederleithinger, E.; Revil, A.; Slater, L.; Williams, K. H.; Orozco, A. F.; Haegel, F.-H.; Hördt, A.; Kruschwitz, S.; Leroux, V.; Titov, K.; Zimmermann, E. An Overview of the Spectral Induced Polarization Method for Near-Surface Applications. *Near Surf. Geophys.* **2012**, *10*, 453–468. https://doi.org/10.3997/1873-0604.2012027.

(23) Feng, L.; Li, Q.; Cameron, S. D.; He, K.; Colby, R.; Walker, K. M.; Deckman, H. W.; Ertaş, D. Quantifying Induced Polarization of Conductive Inclusions in Porous Media and Implications for Geophysical Measurements. *Sci. Rep.* **2020**, *10* (1), 7–11. https://doi.org/10.1038/s41598-020-58390-z.

(24) Placencia-Gómez, E.; Slater, L. D. On the Pore Water Chemistry Effect on Spectral Induced Polarization Measurements in the Presence of Pyrite. *J. Appl. Geophys.* **2016**, *135*, 474–485. https://doi.org/10.1016/j.jappgeo.2015.11.001.

(25) Abdel Aal, G. Z.; Atekwana, E. A.; Revil, A. Geophysical Signatures of Disseminated Iron Minerals: A Proxy for Understanding Subsurface Biophysicochemical Processes. *J. Geophys. Res. Biogeosciences* **2014**, *119*, 1831–1849. https://doi.org/10.1002/2014JG002659.

(26) Gurin, G.; Titov, K.; Ilyin, Y.; Tarasov, A. Induced Polarization of Disseminated Electronically Conductive Minerals: A Semi-Empirical Model. *Geophys. J. Int.* **2015**, *200* (3), 1555–1565. https://doi.org/10.1093/gji/ggu490.

(27) Zhang, C.; Slater, L.; Redden, G.; Fujita, Y.; Johnson, T.; Fox, D. Spectral Induced Polarization Signatures of Hydroxide Adsorption and Mineral Precipitation in Porous Media. *Environ. Sci. Technol.* **2012**, *46* (8), 4357–4364. https://doi.org/10.1021/es204404e.

(28) Izumoto, S.; Huisman, J. A.; Wu, Y.; Vereecken, H. Effect of Solute Concentration on the Spectral Induced Polarization Response of Calcite Precipitation. *Geophys. J. Int.* **2019**, *220*, 1187–1196. https://doi.org/10.1093/gji/ggz515.

(29) de Anna, P.; Jimenez-Martinez, J.; Tabuteau, H.; Turuban, R.; Borgne, T. Le; Derrien, M.; Méheust, Y. Mixing and Reaction Kinetics in Porous Media: An Experimental Pore Scale Quantification. *Environ. Sience Technol.* **2014**, *48*, 508–516. https://doi.org/10.1021/es403105b.

(30) Jiménez-Martínez, J.; Le Borgne, T.; Tabuteau, H.; Méheust, Y. Impact of Saturation on Dispersion and Mixing in Porous Media: Photobleaching Pulse Injection Experiments and Shear-Enhanced Mixing Model. *Water Resour. Res.* **2017**, *53* (2), 1457–1472. https://doi.org/10.1002/2016WR019849.

(31) Jougnot, D.; Jiménez-Martínez, J.; Legendre, R.; Le Borgne, T.; Méheust, Y.; Linde, N. Impact of Small-Scale Saline Tracer Heterogeneity on Electrical Resistivity Monitoring in Fully and Partially Saturated Porous Media: Insights from Geoelectrical Milli-Fluidic Experiments. *Adv. Water Resour.* **2018**, *113*, 295–309. https://doi.org/10.1016/j.advwatres.2018.01.014.

(32) Zimmermann, E.; Kemna, A.; Berwix, J.; Glaas, W.; Münch, H. M.; Huisman, J. A. A High-Accuracy Impedance Spectrometer for Measuring Sediments with Low Polarizability. *Meas. Sci. Technol.* **2008**, *19*, 1–9. https://doi.org/10.1088/0957-0233/19/10/105603.

(33) Wang, C.; Slater, L. D. Extending Accurate Spectral Induced Polarization Measurements into the KHz Range: Modelling and Removal of Errors from Interactions between the Parasitic Capacitive Coupling and the Sample Holder. *Geophys. J. Int.* **2019**, *218* (2), 895–912. https://doi.org/10.1093/gji/ggz199.

(34) Huisman, J. A.; Zimmermann, E.; Esser, O.; Haegel, F.; Treichel, A.; Vereecken, H. Evaluation of a Novel Correction Procedure to Remove Electrode Impedance Effects from Broadband SIP Measurements. *J. Appl. Geophys.* **2016**, *135*, 466–473. https://doi.org/10.1016/j.jappgeo.2015.11.008.

(35) Karadimitriou, N. K.; Hassanizadeh, S. M. A Review of Micromodels and Their Use in Two-Phase Flow Studies. *Vadose Zo. J.* **2012**, *11* (3), vzj2011.0072. https://doi.org/10.2136/vzj2011.0072.

(36) Rolle, M.; Le Borgne, T. Mixing and Reactive Fronts in the Subsurface. *Rev. Mineral. Geochemistry* **2019**, *85* (1), 111–142. https://doi.org/10.2138/rmg.2018.85.5.

(37) Valocchi, A. J.; Bolster, D.; Werth, C. J. Mixing-Limited Reactions in Porous Media. *Transp. Porous Media* **2019**, *130* (1), 157–182. https://doi.org/10.1007/s11242-018-1204-1.

(38) Rodriguez-Navarro, C.; Cara, A. B.; Elert, K.; Putnis, C. V. Direct Nanoscale Imaging Reveals the Growth of Calcite Crystals via Amorphous Nanoparticles. *Cryst. Growth Des.* **2016**, *16*, 1850–1860. https://doi.org/10.1021/acs.cgd.5b01180.

(39) Fernandez-Martinez, A.; Kalkan, B.; Clark, S. M.; Waychunas, G. A. Pressure-Induced Polyamorphism and Formation of 'Aragonitic' Amorphous Calcium Carbonate. *Angew. Chemie* **2013**, *125* (32), 8512–8515. https://doi.org/10.1002/ange.201302974.

(40) Rodriguez-Navarro, C.; Kudłacz, K.; Cizer, Ö.; Ruiz-Agudo, E. Formation of Amorphous Calcium Carbonate and Its Transformation into Mesostructured Calcite. *CrystEngComm* **2015**, *17* (1), 58–72. https://doi.org/10.1039/C4CE01562B.

(41) Leroy, P.; Li, S.; Jougnot, D.; Revil, A.; Wu, Y. Modeling the Evolution of Complex Conductivity during Calcite Precipitation on Glass Beads. *Geophys. J. Int.* **2017**, *209* (1), ggx001. https://doi.org/10.1093/gji/ggx001.

(42) Cole, K. S.; Cole, R. H. Dispersion and Absorption in Dielectrics I. Alternating Current Characteristics. *J. Chem. Phys.* **1941**, *9* (4), 341–351. https://doi.org/10.1063/1.1750906.

(43) Panton, R. L. *Incompressible Flow*, Fourth edi.; John Wiley & Sons, Inc.: Hoboken, New Jersey, 2013. https://doi.org/10.1002/9781118713075.

(44) Zhang, C.; Dehoff, K.; Hess, N.; Oostrom, M.; Wietsma, T. W.; Valocchi, A. J.; Fouke, B. W.; Werth, C. J. Pore-Scale Study of Transverse Mixing Induced CaCO 3 Precipitation and Permeability Reduction in a Model Subsurface Sedimentary System. *Environ. Sci. Technol.* **2010**, *44* (20), 7833–7838. https://doi.org/10.1021/es1019788.

(45) Schwarz, G. A Theory of the Low-Frequency Dielectric Dispersion of Colloidal Particles in Electrolyte Solution. *J. Phys. Chem.* **1962**, *66* (12), 2636–2642. https://doi.org/10.1021/j100818a067.

(46) Lyklema, J.; Dukhin, S. S.; Shilov, V. N. The Relaxation of the Double Layer around Colloidal Particles and the Low-Frequency Dielectric Dispersion. *J. Electroanal. Chem. Interfacial Electrochem.* **1983**, *143*, 1–21. https://doi.org/10.1016/S0022-0728(83)80251-4.

(47) Lesmes, D. P.; Morgan, F. D. Dielectric Spectroscopy of Sedimentary Rocks. *J. Geophys. Res. Solid Earth* **2001**, *106* (B7), 13329–13346. https://doi.org/10.1029/2000jb900402.

(48) Lifshitz, I. M.; Slyozov, V. V. The Kinetics of Precipitation from Supersaturated Solid Solutions. *J. Phys. Chem. Solids* **1961**, *19* (1–2), 35–50. https://doi.org/10.1016/0022-3697(61)90054-3.

(49) Bots, P.; Benning, L. G.; Rodriguez-Blanco, J. D.; Roncal-Herrero, T.; Shaw, S. Mechanistic Insights into the Crystallization of Amorphous Calcium Carbonate (ACC). *Cryst. Growth Des.* **2012**, *12* (7), 3806–3814. https://doi.org/10.1021/cg300676b.

(50) Tarasov, A.; Titov, K. On the Use of the Cole–Cole Equations in Spectral Induced Polarization. *Geophys. J. Int.* **2013**, *195* (1), 352–356. https://doi.org/10.1093/gji/ggt251.

(51) Arcone, S. A.; Boitnott, G. E. Complex Permittivity of Common Minerals and One Soil at Low Water Contents. In *Proceedings of the XIII Internarional Conference on Ground Penetrating Radar*; IEEE, 2010; pp 1–6. https://doi.org/10.1109/ICGPR.2010.5550133.

(52) Bresciani, E.; Kang, P. K.; Lee, S. Theoretical Analysis of Groundwater Flow Patterns Near Stagnation Points. *Water Resour. Res.* **2019**, *55* (2), 1624–1650. https://doi.org/10.1029/2018WR023508.